Contributions of dielectronic, trielectronic, and metastable channels to the resonant intershell recombination of highly charged silicon ions

Thomas M. Baumann,[1,2,*] Zoltán Harman,[1,3] Julian Stark,[1] Christian Beilmann,[1,†] Guiyun Liang,[4] Paul H. Mokler,[1] Joachim Ullrich,[5] and José R. Crespo López-Urrutia[1,‡]

[1]*Max-Planck-Institut für Kernphysik, Saupfercheckweg 1, 69117 Heidelberg, Germany*

[2]*National Superconducting Cyclotron Laboratory, Michigan State University, 640 South Shaw Lane, East Lansing, Michigan 48824, USA*

[3]*ExtreMe Matter Institute EMMI, Planckstrasse 1, 64291 Darmstadt, Germany*

[4]*Key Laboratory of Optical Astronomy, National Astronomical Observatories, CAS, Beijing, China*

[5]*Physikalisch-Technische Bundesanstalt, Bundesallee 100, 38116 Braunschweig, Germany*

(Received 5 July 2013; revised manuscript received 16 September 2014; published 7 November 2014)

Intershell, resonant electronic recombination is studied experimentally in an electron-beam ion trap for O-like Si^{6+} to He-like Si^{12+} ions at plasma temperatures in the megakelvin range similar to those found in the solar radiative zone and is compared to extended multiconfiguration Dirac-Fock and relativistic configuration-interaction predictions. For this low-Z ion, the higher-order electronic recombination processes are comparable in strength to the first-order one. The ratio of trielectronic to dielectric recombination for B-like species agrees well with predictions, whereas for C-like ions the measured value is only half as large. This difference is explained by the influence of metastable states populated in the recombining plasma.

DOI: 10.1103/PhysRevA.90.052704 PACS number(s): 34.80.Lx, 32.30.Rj, 52.25.Os

I. INTRODUCTION

The major part of all visible baryonic matter in the universe is highly ionized with stellar plasmas as the most obvious concentrations. The underlying fundamental atomic processes determining the plasma conditions in astrophysical objects are photon-electron and electron-electron interactions. We focus our investigation on resonant electronic recombination processes [1] in which a free electron is captured under excitation of one or more bound electrons, populating an intermediate, multiply excited state that stabilizes through photon emission. The basic first-order recombination case, the interaction of two electrons (one free and one bound), is just the time reversal of a photon-excited state decaying via Auger processes [2]. Hence, we use the Auger nomenclature analogously, with, e.g., K-LL dielectronic recombination (DR) meaning a resonant capture to the L shell under the excitation of a K electron to the L shell.

The next-higher-order electronic recombination process, trielectronic recombination (TR) is the capture of one electron under excitation of two bound electrons. It was first found in highly charged species of medium heavy ions in a storage ring measurement by Schnell *et al.* [3]. Those observations showed *intrashell* excitations resulting from low-energy (a few eV) collisions. More recently, unexpectedly strong contributions of *intershell* TR processes at keV collision energies were found in electron-beam ion-trap measurements [4–6]. They may even exceed the strength of DR in ions with atomic numbers $Z < 20$. For instance, for K-L excitation in C-like Ar ($Z = 18$) ions a strength ratio of $S^{\mathrm{TR}}/S^{\mathrm{DR}} = 1.4$ was found. These strong effects will influence the ionization degree and the cooling of plasmas containing such ions. In particular, the Rosseland mean opacities of these plasmas used in radiative-collisional codes have to be revised to include them [7,8].

The element under study in our investigation, silicon ($Z = 14$), is the eighth most abundant element in the solar chemical composition and contributes about 9% to the total opacity of the solar radiative zone [9,10]. Electron-electron correlation is comparatively strong in low-Z atoms and thus the strength of TR is predicted to rise further when going down in Z from Ar to Si [5]. At very low Z the decrease of radiative decay probabilities frustrates the completion of the recombination process and therefore a maximum of the $S^{\mathrm{TR}}/S^{\mathrm{DR}}$ value should appear. The goal of the present investigation is to find the $S^{\mathrm{TR}}/S^{\mathrm{DR}}$ ratio in the low-Z highly charged Si ions. Dielectronic recombination in Si has been studied in detail at low collision energies in storage ring measurements (e.g., [11–16]). There are only few data on the K-LL region: a storage ring measurement on Li-like Si [17] and a study on H- and He-like Si [18]. The inverse process, namely, K-shell photoabsorption in Si ions and its influence on solar opacities, is studied in [19] using a laser produced plasma. We present high-resolution measurements on the K-LL recombination in He- to O-like silicon.

II. THEORY

In the case of DR, a free electron is captured by an ion in the initial state $|i\rangle$ under excitation of a bound electron, forming an excited intermediate state $|d\rangle$ that decays to a final state $|f\rangle$ under photon emission to complete the recombination process. Here we focus on the K-LL recombination involving $n = 1 \rightarrow n = 2$ excitations and recombination also into the $n = 2$ shell. The resonance strength S^{DR} of this process can be calculated from the DR cross section $\sigma_{\mathrm{DR}}(E)$, which depends on the electron kinetic energy E, from (see, e.g., [20])

$$S^{\mathrm{DR}} = \int \sigma_{\mathrm{DR}}(E)dE = \frac{2\pi^2\hbar^3}{p^2}\frac{g_d}{g_i}\frac{A^{\mathrm{a}}_{d\rightarrow i}\sum_f A^{\mathrm{r}}_{d\rightarrow f}}{\sum_i A^{\mathrm{a}}_{d\rightarrow i} + \sum_f A^{\mathrm{r}}_{d\rightarrow f}}. \quad (1)$$

*baumannt@nscl.msu.edu

†Present address: Karlsruhe Institute of Technology, Hermann von-Helmholtz-Platz 1, 76344 Eggenstein-Leopoldshafen, Germany.

‡crespojr@mpi-hd.mpg.de

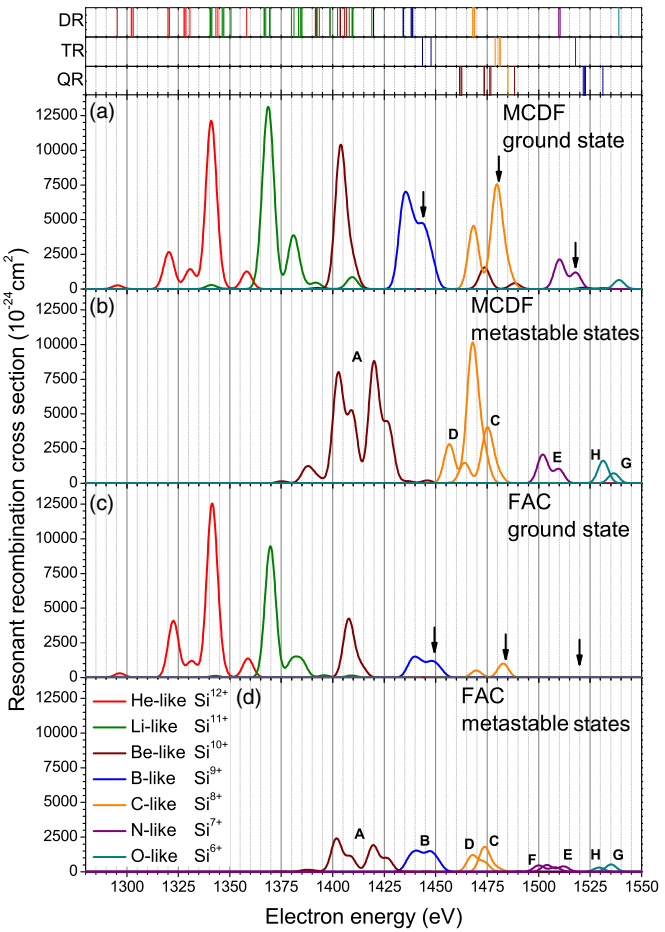

FIG. 1. (Color online) Results of the MCDF and FAC calculations for different charge states. The predicted resonance strengths are convolved with a 6-eV-wide Gaussian line profile to account for experimental resolution. (a) and (c) show the recombination resonances into ions in the ground state, while (b) and (d) consider recombination into ions in initially excited metastable states. The top bar code panel indicates the recombination order according to the MCDF calculation. Black arrows mark TR resonances. The labels for the metastable states are given in Table I. The B-like MSs are not included in the MCDF calculation.

Here the momentum p of the recombining electron, as well as the statistical weights of the initial and excited intermediate states g_i and g_d, and the radiative rates $A^{\mathrm{r}}_{d\to f}$ for the deexcitation of the intermediate state $|d\rangle$ to the final state $|f\rangle$ and the autoionization rate $A^{\mathrm{a}}_{d\to i}$ are used.

For a theoretical treatment to include higher-order recombination, electron-electron interactions have to be judiciously taken into account. In this work, two fully relativistic calculations were performed: a multiconfiguration Dirac-Fock (MCDF) calculation [21–23] and a relativistic configuration-interaction calculation using the Flexible Atomic Code (FAC) [24,25]. The results of our calculations are shown in Fig. 1 as well as in Tables IV–VIII and IX–XII in the Appendix.

Only ions in the ground state were considered as the initial state $|i\rangle$ for the calculations labeled ground state (g.s.). A second calculation was performed for recombination into ions

TABLE I. Initial states considered in the FAC and MCDF calculations for the different Si charge states. For the metastable states, the energy difference to the ground state is given (resulting from the FAC). Metastable state lifetimes are taken from experimental data (see [26]) or are estimated using FAC radiative transition rates (and marked with an asterisk). The ground states are marked g.s. and metastable states are labeled with letters that are also used in Fig. 1.

Charge state	Level		Energy (eV)	Lifetime (ms)	Label
He-like	Si^{12+}	$1s^2\,{}^1S_0$	0		g.s.
Li-like	Si^{11+}	$1s^2 2s^1\,{}^2S^o_{1/2}$	0		g.s.
Be-like	Si^{10+}	$1s^2 2s^2\,{}^1S_0$	0		g.s.
Be-like	Si^{10+}	$1s^2 2s 2p\,{}^3P^o_0$	21.3	very long	*A*
B-like	Si^{9+}	$1s^2 2s^2 2p\,{}^2P^o_{1/2}$	0		g.s.
B-like	Si^{9+}	$1s^2 2s^2 2p\,{}^2P^o_{3/2}$	0.9	345*	*B*
C-like	Si^{8+}	$1s^2 2s^2 2p^2\,{}^3P_{0,1,2}$	0		g.s.
C-like	Si^{8+}	$1s^2 2s^2 2p^2\,{}^1D_2$	6.8	38.3	*C*
C-like	Si^{8+}	$1s^2 2s^2 2p^2\,{}^1S_0$	12.9	5*	*D*
N-like	Si^{7+}	$1s^2 2s^2 2p^3\,{}^4S^o_{3/2}$	0		g.s.
N-like	Si^{7+}	$1s^2 2s^2 2p^3\,{}^2D^o_{3/2,5/2}$	8.9	9.6	*E*
N-like	Si^{7+}	$1s^2 2s^2 2p^3\,{}^2P^o_{1/2,3/2}$	12.9	23.5	*F*
O-like	Si^{6+}	$1s^2 2s^2 2p^4\,{}^3P_{2,1,0}$	0		g.s.
O-like	Si^{6+}	$1s^2 2s^2 2p^4\,{}^1D_2$	5.9	63.6	*G*
O-like	Si^{6+}	$1s^2 2s^2 2p^4\,{}^1S_0$	11.8	8*	*H*

in excited initial states labeled metastable states (MSs) in Fig. 1. These are low-lying excited states, only decaying through forbidden transitions with lifetimes on the order of several tens of ms [26] for C-, N-, and O-like Si. These lifetimes are similar to the experimental time scales and can have an impact on the measurement. The states used in the calculation are summarized in Table I.

First, we compare the MCDF and FAC calculations for recombination into the ground state. While both agree within their uncertainties of 5 eV for the resonance energies, there are large differences concerning the resonance strengths. Both methods deliver similar results for He-like and Li-like silicon. For Be-like silicon there is already a factor of 2 difference between the FAC and MCDF resonance strength results. This difference increases further for lower charge states. Astonishingly, the FAC yields N-like and O-like Si results that are four orders of magnitude below those for the C-like ions. This strong drop results from a similar decrease of the autoionization rates $A^{\mathrm{a}}_{d\to i}$ for N- and O-like Si in the calculation. We could not find an explanation for this strong drop, which is not reproduced in MCDF calculations. The sums over all DR and TR contributions for B-like to N-like Si are given in Table II. The ratio between the total TR and DR contributions is referred to as $S^{\mathrm{TR}}/S^{\mathrm{DR}}$ in the following.

The MCDF calculation shows a very strong contribution of quadruelectronic recombination (QR) (the next-higher-order recombination process, involving the excitation of three electrons) into Be-like silicon at an energy of 1473 eV, which lies in the region of the C-like DR and TR resonances. The FAC calculates a QR resonance strength three orders of magnitude below the MCDF result.

TABLE II. Total recombination strength summed over all TR and DR contributions for the given charge states, calculated from the MCDF calculation and the FAC, in units of barn eV. The ratio of these sums, which is called S^{TR}/S^{DR} in the text, is given in the columns labeled "Ratio."

	MCDF			FAC		
Ion	$\sum S^{DR}$	$\sum S^{TR}$	Ratio	$\sum S^{DR}$	$\sum S^{TR}$	Ratio
B-like	2.44×10^5	1.43×10^5	0.59	5.18×10^4	3.78×10^4	0.73
C-like	1.18×10^5	2.05×10^5	1.75	1.31×10^4	2.62×10^4	2.00
N-like	5.48×10^4	3.02×10^4	0.55	1.20×10^1	1.28×10^1	1.07

The theoretical spectra for recombination into ions in excited metastable states show resonance strengths of the same magnitude as that of ground-state recombination. They appear at lower collision energies due to the higher initial energy of the MSs. Thus, when long-lived MSs are significantly populated in the plasma, their effect on resonant recombination spectra has to be taken into account.

III. EXPERIMENTAL SETUP

In highly charged Si ions the fine-structure splitting is small, thus the recombination resonances are closely spaced, requiring a high-energy resolution to resolve. The experiment was performed on ions under very well controlled experimental conditions within an electron-beam ion trap (EBIT) recently commissioned at the Max Planck Institute for Nuclear Physics, dubbed HYPER-EBIT.

The experimental arrangement is similar to earlier work at Lawrence Livermore National Laboratory [27] and elsewhere [28,29] but also includes strong continuous evaporation for ion cooling, as in the work of Beilmann *et al.* [5]. A scheme of the setup is shown in Fig. 2. Silicon is injected into the EBIT via the gas injection system using a monosilane (SiH_4) gas jet. The silane molecules are instantly broken by the electron beam and the silicon ionization process starts. The electron-beam energy is ramped linearly between 1280 and 1580 eV by changing V_{cath}, while the recombination resonances are probed with an x-ray detector registering characteristic radiation emitted during radiative stabilization of the intermediate states. Carefully controlled electron-beam conditions at relatively low beam currents between 10 and 50 mA were used in several runs. A slow beam energy ramp (about 1 eV/s) together with the strong evaporative cooling resulting from a very shallow axial trapping potential V_{DT} of a few volts yields an electron-beam energy resolution of 6 eV and below, which is excellent at resonance energies around 1.5 keV. The electron-beam current I was controlled to rise proportionally to the electron energy in a way that the electron-beam space-charge potential $V_{SC} \propto I/\sqrt{V_{trap} - V_{cath}}$ was kept constant during the scans. For x-ray detection, we used a commercial silicon-drift detector (AmpTek XR-100SDD) with an area of 25 mm^2, giving a detection solid angle of 5.3×10^{-3} sr and an energy resolution of 130 eV at 1.8 keV photon energy.

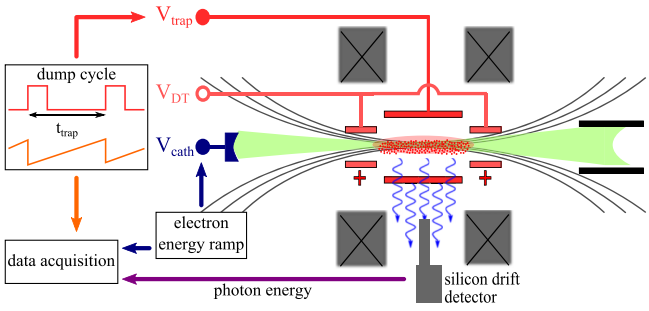

FIG. 2. (Color online) Scheme of the experimental setup. The electron-beam energy is ramped slowly by changing V_{cath} with about 1 V/s, while the trap region is biased on the positive potential V_{trap}. This potential is increased in regular 250-ms-long intervals to empty the trap and to restart the charge breeding process. The voltage V_{DT} defines the axial trapping potential. The recombination x-ray photons are detected by a silicon drift detector. Signals proportional to the electron-beam energy and the time within the dump cycle, as well as the detector output, are fed into the data acquisition system.

In addition, the time evolution of the ion charge state was monitored in the following way. The trap is emptied from all ions (so-called dump) at regular intervals by applying a high-voltage pulse on the central trap electrode (see Fig. 2). Afterwards, ion production and accumulation restarts with typical total trapping times between $t_{trap} = 250$ and 700 ms. For each detected photon event, the electron and photon energies as well as the time within the dump cycle t_d are recorded.

IV. RESULTS AND DISCUSSION

A. Time evolution

In the top panel of Fig. 3, the K-LL photon yield is depicted as a function of both the energy of the recombining electron E_e and the detection time within the dump cycle t_d for a measurement using 50 mA of electron-beam current. During the first 20 ms the trap is open and no highly charged ions are produced. After closing it, ions accumulate and can be detected by their characteristic recombination photon emission. Recombining O- to He-like silicon ions dominate at different charge breeding times. The resonances of these species are marked.

To analyze this measurement, we carry out a simulation of the charge state evolution (see, e.g., [30]) at a given current density j, solving the system of coupled differential equations

$$\frac{d}{dt}n_q = \frac{j}{e}\left[\sigma^{EII}_{q-1}(E)n_{q-1} + \sigma^{rec}_{q+1}(E)n_{q+1} - \sigma^{EII}_{q}(E)n_q - \sigma^{rec}_{q}(E)n_q\right]. \quad (2)$$

It includes the energy-dependent cross sections for electron-impact ionization $\sigma^{EII}_q(E)$ and radiative and resonant

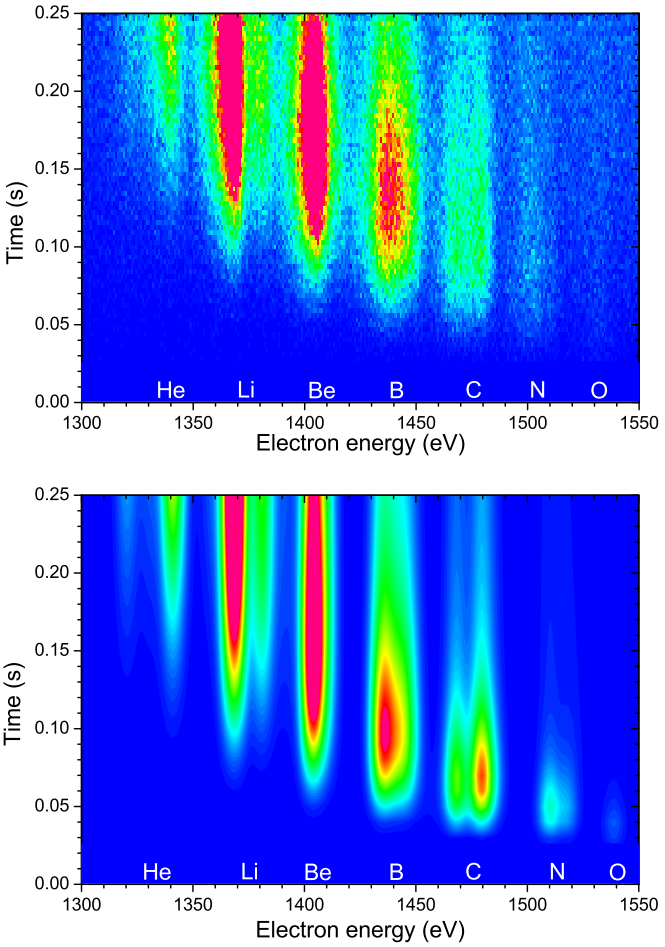

FIG. 3. (Color online) Evolution of the recombination resonances dependent on the dump cycle time t_d. The top shows the measured data and the bottom the results of the simulation based on MCDF data. The appearance of resonant recombination features in the spectrum is governed by the evolution of the charge states of ions during the cycle.

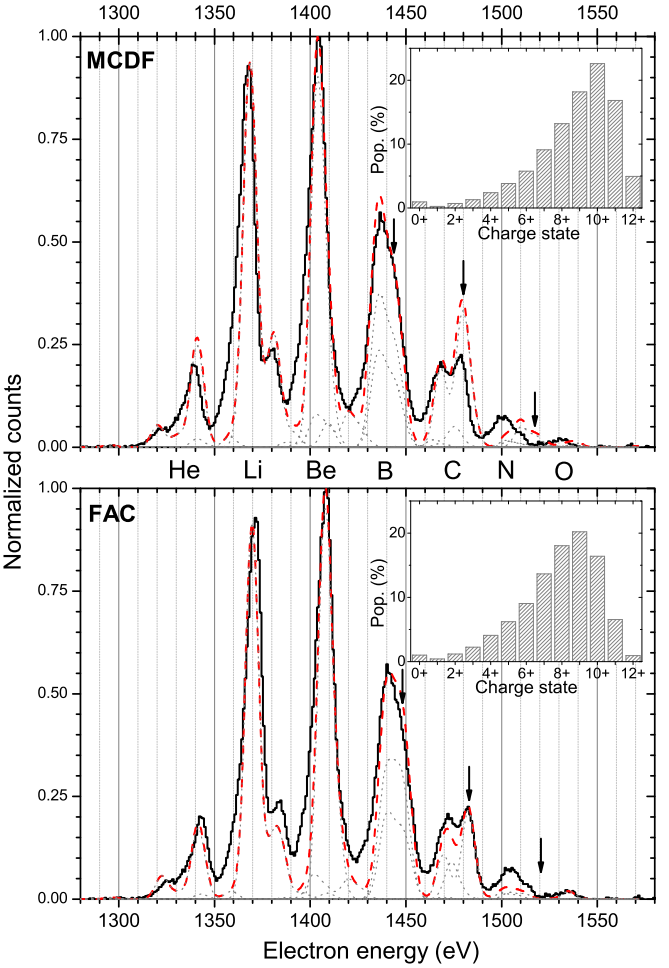

FIG. 4. (Color online) Time-integrated recombination spectra dependent on the electron-beam energy. The results of the MCDF and FAC calculations, including recombination into metastable levels, which are weighted by the simulated charge state distribution, are shown for comparison (the red dashed line shows the summed spectrum and the gray dotted line the individual contributions). In the upper right corner of each plot, the resulting charge state distribution (population in percent) is shown for a current density of $j = 14$ A/cm^2 for the MCDF calculation and $j = 8.4$ A/cm^2 for the FAC.

recombination $\sigma_q^{\mathrm{rec}}(E)$, ignoring losses due to charge exchange or ion escape from the trap. Furthermore, a term describing a constant neutral gas injection is included in the equation for $q = 1$. The cross sections for resonant recombination are taken from the MCDF calculation and for the other processes from the FAC. The results of the simulation are shown in the lower panel of Fig. 3.

Ions in excited metastable levels are accounted for in the calculation by splitting the population n_q into populations n_q^i for each sublevel i shown in Table I. Their populations are modeled by including weighting factors r_q^i in the terms for the ionization process $\frac{d}{dt}n_q^i = \frac{j}{e}r_q^i\sigma_{q-1}^{\mathrm{EII}}(E)n_{q-1}$. The factors r_q^i are result from the multiplicities of the levels. Furthermore, the decay of metastable levels into their ground state is included using the their lifetime by $\frac{d}{dt}n_q^i = \frac{1}{\tau_q^i}n_q^i$.

It is apparent from Fig. 3, where the results of our simulation are shown together with the experimental observations, that the ion charge state grows with time. The (MCDF-based) simulation agrees well with the data if an effective electron current density of $j = 14$ A/cm^2 is used. Furthermore, this time-evolution measurement delivers a deep insight into the processes inside the trap and allows for the optimization of operation parameters as well as the removal of systematic error sources.

B. Recombination spectra

Figure 4 shows the measured recombination resonances projected on the electron energy axis after integration over the total measurement time in comparison to the MCDF and FAC results. Since the electron-beam space charge is kept constant, the energy rises linearly with acceleration potential and the energy scale needs a single resonance as reference, in the present case the theoretical prediction of the Be-like resonance. For comparison, the experimental intensities are normalized to the Be-like resonance. The predicted resonance strengths are weighted by the simulated charge state distribution (which is shown in the upper right corner of each spectrum) and

normalized to the Be-like resonance. In both simulations different electron-beam current densities are used for better agreement with the observations. The charge state simulation based on MCDF cross sections uses $j = 14$ A/cm^2, while the FAC simulation needs $j = 8.4$ A/cm^2. Recombination into the ground state as well as metastable levels are included in the calculations, which agree in general well with the data, but significant deviations are also found.

The relatively low current density results from the choice of a weak electron beam and the corresponding large expansion of the ion ensemble, which overlaps only fractionally (see, e.g., [31]) with the electron beam. The low total charges of the Si ions are also a factor here since they experience a weaker trapping potential. The low current density was chosen intentionally to increase the yield of relatively low charge states (mainly C-like Si) for the recombination measurement. The current densities correspond to an effective electron density of $n_e = 2.3 \times 10^{10}$ cm^{-3} for the FAC and $n_e = 3.8 \times 10^{10}$ cm^{-3} for the MCDF calculation. Experimentally, an electron-beam density of $n_e = 2.2 \pm 1.3 \times 10^{10}$ cm^{-3} was determined during one of the DR measurement runs, which is compatible with the theoretically obtained values. For this, a grating spectrometer, which is sensitive in the extreme ultraviolet spectral region between 5 and 35 nm, was used by comparing the line ratios of two density-sensitive transitions in Ne-like silicon [32].

The KLL resonant recombination in highly charged He- to O- like Si ions was measured with a relatively high resolution of 6 eV in the energy of the projectile electron. The dependences of the resonances on electron and photon energies as well as the time during the EBIT trapping cycle were recorded, which allows for a direct observation of the charge breeding process in the trap. The results were compared to the predictions of a MCDF and a FAC calculation combined with a charge state evolution simulation.

We found good agreement of theory with the experimental results for the high-charge and few-electron systems. For lower-charge states, deviations were observed. We focused on the strength ratio of the TR and DR peaks in C-like silicon, which was observed to be 1.14 ± 0.13. This ratio could be explained by an influence of recombination into excited, long-living levels in C-like Si.

For a further test, we compare the measured photon energies with the results of the MCDF calculations. In principle, the silicon-drift detector has a resolution of 130 eV only, which is not sufficient to resolve the transitions excited by recombination of the different charge states. However, we can separate these peaks by using the electron-beam energy information to discriminate the data. The results of a fit to the photon peaks for the recombination into different charge states of silicon are summed up in Table III.

TABLE III. Measured and calculated photon energies for the relaxation of the strongest dielectronic resonances of the different charge states.

	Photon energy (eV)	
$\|i\rangle$	Experiment	MCDF
He-like	1848.8 (4.4)	1843.7
Li-like	1823.3 (1.4)	1823.3
Be-like	1805.3 (2.0)	1806.0
B-like	1790.9 (2.1)	1788.8
C-like DR	1772.9 (2.4)	1772.7
C-like TR	1774.0 (2.6)	1771.4
N-like	1754.3 (4.4)	1756.6

C. Role of metastable states

The inclusion of recombination into the MS $1s^2 2s 2p\ ^3P_0^o$ level in Be-like Si (see Table I label *A*) improves the calculation in the region around 1420 eV. The theoretical predictions for recombination into the g.s. of N-like and O-like charge states disagrees with the measured energies by about 10 eV. Here the FAC calculation deviates in the resonance strength due to the very low cross sections applied for recombining into the g.s., as mentioned above, but reproduces the resonance energy better than the MCDF calculation.

The B-like recombination resonance consists of two contributions at the given experimental resolution: a DR resonance at 1435 eV and the higher-order TR resonance at 1443 eV. In this region, no contributions from other charge states are expected. In spite of their small separation in comparison with the C-like resonances, a fit of two Gaussian distributions can still be applied. Averaging over all data sets, we get a ratio of $S^{\mathrm{TR}}/S^{\mathrm{DR}} = 0.7 \pm 0.1$. The MCDF calculation predicts a ratio of 0.59 for recombination into the B-like g.s. configuration $1s^2 2s^2 2p\ ^2P_{1/2}$, while the FAC gives a ratio of 0.73. Both are consistent with the measured value.

D. TR and DR in C-like Si

In the following, we concentrate on recombination into C-like silicon. At the given experimental energy resolution, two resonances arise from this recombination, one DR peak around 1468 eV and a TR peak at 1480 eV. For a low-Z ion like Si, TR is expected to be nearly twice as strong as DR, with $S^{\mathrm{TR}}/S^{\mathrm{DR}} = 1.75$ in the MCDF calculation. The FAC calculation predicts an even stronger TR contribution and yields $S^{\mathrm{TR}}/S^{\mathrm{DR}} = 2.0$. In earlier measurements of Kr ($Z = 36$), Fe ($Z = 26$), and Ar ($Z = 18$), this strong TR influence and the trend of increased TR toward lower Z was confirmed [5].

However, our Si measurement shows a strength ratio of $S^{\mathrm{TR}}/S^{\mathrm{DR}} = 1.14 \pm 0.13$. This value is obtained by averaging over all data sets. Both calculations strongly deviate from this value.

One reason for this deviation can be the recombination into long-living excited states. We calculated the recombination into the excited $1s^2 2s^2 2p^2\ ^1D_2$ and $1s^2 2s^2 2p^2\ ^1S_0$ levels in addition to the ground state $1s^2 2s^2 2p^2\ ^3P_0$. The ratio of the two observed resonances can strongly be influenced by the recombination into these metastable states, if sufficiently populated. They have lifetimes in the ms range (see Table I), which are comparable to the experimental time scale, considering that the recombination into C-like Si dominates the spectrum for about 60 ms. The cross sections for a collisional excitation of the MS $1s^2 2s^2 2p^2\ ^1D_2$ and $1s^2 2s^2 2p^2\ ^1S_0$ levels from the $1s^2 2s^2 2p^2\ ^3P_0$ ground state were estimated to be 3×10^{-21} and 4×10^{-22} cm^2, respectively, at an electron

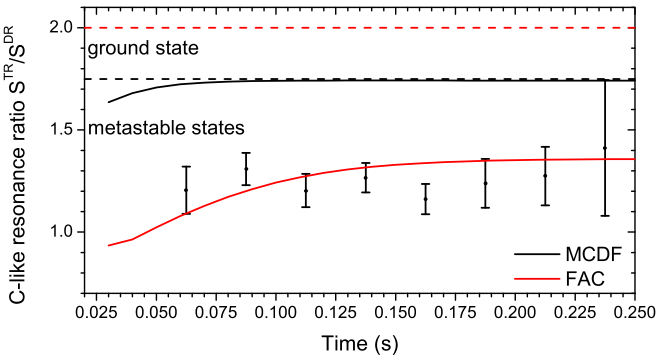

FIG. 5. (Color online) Comparison between the measured time evolution of the C-like resonance ratio and the result of the simulation. The simulation uses the MCDF or FAC results and includes only recombination into the ground state for the dashed line and also recombination into metastable levels for the solid line.

energy of 1450 eV using the FAC [25]. This is nearly three orders of magnitude lower than the collisional ionization cross sections. Thus a population of these levels cannot be explained by collisional excitation [33], but has to be a result of an ionization process. In our simulation, we assume a statistical population distribution after ionization of 3/15 in each of the ^3P terms, 5/15 in the ^1D term, and 1/15 in the ^1S term. Resonant recombination into the resulting state distribution leads to a significant decrease of the C-like resonance ratio.

The time evolution of the ratio is shown in Fig. 5. The points are the result of a fit to the measured TR and DR resonances, which were integrated over 25-ms-long nonoverlapping intervals. These points are compared to simulations, including the MCDF or FAC results of recombination into the ground state and into the aforementioned excited states. It is evident that the inclusion of metastable levels decreases the theoretical ratio to values that are in better agreement with the data in the case of the FAC calculation. The MCDF calculation still cannot reproduce the measured ratio, but also shows the tendency towards lower ratios.

The MCDF calculation predicts, unlike the FAC, a very strong resonance at 1473 eV that results from third-order recombination (QR) into Be-like Si ions. This resonance cannot be observed at the predicted strength; however, if it is present with a lower resonance strength, it might still have an influence on the observable C-like ratio. Another problem is that the ratio is very sensitive to the energies of the contributing transitions. Within the same charge state, the contributions can be calculated quite accurately, but relative to different charge states, the accuracy of the MCDF and FAC calculations is only a few eV.

V. CONCLUSION

In conclusion, the K-LL resonant recombination in highly charged He-like to O-like Si ions was measured and compared to the predictions of the MCDF and FAC calculations combined with charge state evolution simulations. We found good agreement of theory with the experimental results for the ions having fewer than six bound electrons. However, significant deviations were observed on the strength ratio of the TR and DR resonances in C-like silicon. This discrepancy can be reduced if recombination into excited, long-lived metastable levels is included in the calculations.

The general trend of strong contributions from trielectronic processes in the K-LL resonance region is further established. About 20% of the detected recombination photons from all charge states at the EBIT plasma conditions in the here presented measurement arise from higher-order recombination. Based on detailed balance, the

TABLE IV. Resonance energies E_e and resonance strengths S^{rec} for resonant recombination into the ground state of He-like silicon ions according to MCDF and FAC calculations. Here J denotes the total angular momentum of the autoionizing state $|d\rangle$.

			MCDF results		FAC results	
$\|i\rangle$	$\|d\rangle$	J	E_e (eV)	S^{rec} (b eV)	E_e (eV)	S^{rec} (b eV)
He	$1s2s^2$	1/2	1295.4	6.74×10^3	1296.5	7.81×10^3
He	$1s2s2p$	1/2	1302.1	1.54×10^1	1302.1	1.89×10^1
He	$1s2s2p$	3/2	1302.4	1.85	1302.3	2.00×10^{-2}
He	$1s2s2p$	5/2	1303.1	3.76×10^{-1}	1303.0	3.90×10^{-1}
He	$1s2s2p$	1/2	1320.0	3.31×10^4	1322.3	4.7×10^4
He	$1s2s2p$	3/2	1320.7	3.57×10^4	1322.8	5.79×10^4
He	$1s2p^2$	1/2	1327.8	4.83×10^{-1}	1327.8	1.03
He	$1s2p^2$	3/2	1328.2	6.49×10^1	1328.2	5.33×10^1
He	$1s2p^2$	5/2	1328.7	4.99×10^2	1328.7	4.44×10^2
He	$1s2s2p$	1/2	1330.6	1.66×10^4	1331.3	1.50×10^4
He	$1s2s2p$	3/2	1330.7	1.96×10^4	1331.6	1.52×10^4
He	$1s2p^2$	5/2	1340.8	1.78×10^5	1341.2	1.87×10^5
He	$1s2p^2$	3/2	1340.9	1.24×10^5	1341.4	1.29×10^5
He	$1s2p^2$	1/2	1343.3	2.42×10^2	1344.4	2.59×10^2
He	$1s2p^2$	3/2	1344.2	3.24×10^4	1345.4	1.76×10^4
He	$1s2p^2$	1/2	1358.2	3.24×10^4	1358.7	3.51×10^4

effects of these recombination resonances and of their corresponding photoionization resonances significantly influence the photon scattering rate and the plasma conditions such as ionization balance and charge state distribution in general.

Given the abundance of medium heavy elements with open L shells in the solar radiative zone, these complex TR resonances need to be calculated in more detail in order to improve the quality of Rosseland mean opacities. Furthermore, the role of metastable states and their strongly correlated TR resonances is shown to have an impact on plasma models. Since actual plasma in the solar radiative zone may contain significant populations of such ions, the observed effects point to the need of upgrading current collisional-radiative codes used for opacity calculations.

ACKNOWLEDGMENTS

The work of Z.H. was supported by the Alliance Program of the Helmholtz Association (HA216/EMMI). G.Y.L. was supported by the National Natural Science Foundation of China (Grant No. 11273032).

APPENDIX

In this Appendix we present theoretical resonance energies and recombination resonance strengths for all the charge states of Si. Tables IV–VIII contain results for the ions being in their ground state before recombination, while Tables IX–XII are for ions initially in metastable valence-excited states.

TABLE V. Same as Table IV for Li-like ions.

			MCDF results		FAC results	
$\|i\rangle$	$\|d\rangle$	J	E_e (eV)	S^{rec} (b eV)	E_e (eV)	S^{rec} (b eV)
Li	$1s2s^22p$	0	1340.4	7.92×10^2	1342.3	3.38×10^2
Li	$1s2s^22p$	1	1340.6	2.72×10^3	1342.5	1.15×10^3
Li	$1s2s^22p$	2	1341.4	4.11×10^3	1343.2	1.73×10^3
Li	$1s2s2p^2$	1	1346.3	2.95×10^1	1346.1	2.62×10^1
Li	$1s2s2p^2$	2	1346.7	2.24×10^1	1346.5	1.45×10^1
Li	$1s2s2p^2$	3	1347.1	7.23×10^1	1346.9	6.46×10^1
Li	$1s2s^22p$	1	1350.5	7.78×10^2	1353.5	2.81×10^2
Li	$1s2s2p^2$	0	1366.6	1.08×10^2	1369.9	6.26×10^1
Li	$1s2s2p^2$	1	1366.9	5.43×10^4	1369.6	4.51×10^4
Li	$1s2s2p^2$	2	1367.5	9.90×10^4	1369.5	7.03×10^4
Li	$1s2s2p^2$	3	1369.3	9.44×10^4	1369.5	8.99×10^4
Li	$1s2s2p^2$	2	1369.5	7.13×10^4	1370.9	1.88×10^4
Li	$1s2s2p^2$	1	1369.6	4.73×10^4	1370.3	2.16×10^4
Li	$1s2s2p^2$	1	1380.0	3.48×10^4	1380.2	3.04×10^4
Li	$1s2p^3$	2	1381.2	6.43×10^4	1384.8	2.75×10^4
Li	$1s2s2p^2$	2	1383.4	2.42×10^1	1382.5	4.82
Li	$1s2s2p^2$	0	1384.2	2.14×10^2	1385.0	2.58
Li	$1s2s2p^2$	1	1384.6	1.38×10^3	1385.4	1.51×10^1
Li	$1s2s2p^2$	2	1385.0	8.34×10^3	1385.9	1.68×10^3
Li	$1s2s2p^2$	0	1391.9	1.15×10^4	1395.8	4.16×10^3
Li	$1s2s2p^2$	1	1393.4	8.62×10^1	1394.0	3.66×10^1
Li	$1s2p^3$	2	1398.8	7.91×10^1	1398.4	6.25
Li	$1s2p^3$	1	1398.8	2.59×10^1	1398.4	2.02
Li	$1s2p^3$	1	1402.3	5.31×10^1	1403.1	5.02×10^1
Li	$1s2p^3$	2	1408.0	4.15×10^3	1408.3	8.81×10^2
Li	$1s2p^3$	1	1409.4	7.12×10^3	1409.1	1.09×10^3
Li	$1s2p^3$	0	1409.6	2.33×10^3	1409.2	3.51×10^2
Li	$1s2p^3$	2	1409.6	9.20×10^3	1409.4	1.65×10^3
Li	$1s2p^3$	1	1418.9	6.29×10^1	1419.4	6.72

TABLE VI. Same as Table IV for Be-like ions. Higher-order (HO) recombination channels are marked by TR (trielectronic) or QR (quadruelectronic).

				MCDF results		FAC results	
$\|i\rangle$	$\|d\rangle$	J	HO	E_e (eV)	S^{rec} (b eV)	E_e (eV)	S^{rec} (b eV)
Be	$1s2s^22p^2$	1/2		1391.5	2.71×10^2	1395.2	1.17
Be	$1s2s^22p^2$	3/2		1391.9	5.55×10^1	1395.6	7.68×10^{-2}
Be	$1s2s^22p^2$	5/2		1392.3	1.65×10^3	1396.1	4.56
Be	$1s2s^22p^2$	5/2		1403.6	1.48×10^5	1407.5	6.19×10^4
Be	$1s2s^22p^2$	3/2		1403.7	1.03×10^5	1407.6	4.26×10^4
Be	$1s2s^22p^2$	1/2		1405.8	4.71×10^3	1410.1	2.44×10^3
Be	$1s2s^22p^2$	3/2		1406.7	1.74×10^4	1411.0	3.73×10^3
Be	$1s2s^22p^2$	1/2		1409.7	4.44×10^4	1413.7	1.93×10^4
Be	$1s2p^4$	5/2	QR	1461.6	8.49×10^1	1465.8	6.07×10^{-2}
Be	$1s2p^4$	3/2	QR	1462.3	1.93×10^1	1466.6	1.05×10^{-2}
Be	$1s2p^4$	1/2	QR	1462.6	1.60×10^1	1466.9	1.58×10^{-1}
Be	$1s2p^4$	5/2	QR	1473.5	2.40×10^4	1477.8	8.59
Be	$1s2p^4$	3/2	QR	1473.6	1.55×10^4	1477.9	5.75
Be	$1s2p^4$	3/2	QR	1476.2	4.95×10^2	1480.5	4.94×10^{-1}
Be	$1s2p^4$	1/2	QR	1476.8	4.74×10^1	1481.1	8.46×10^{-1}
Be	$1s2p^4$	1/2	QR	1488.2	1.08×10^4	1492.5	1.30×10^2

TABLE VII. Same as Table VI for B-like ions.

				MCDF results		FAC results	
$\|i\rangle$	$\|d\rangle$	J	HO	E_e (eV)	S^{rec} (b eV)	E_e (eV)	S^{rec} (b eV)
B	$1s2s^22p^3$	2		1419.8	7.69×10^1	1424.0	2.85×10^{-2}
B	$1s2s^22p^3$	3		1434.2	6.24×10^4	1438.3	7.95×10^3
B	$1s2s^22p^3$	2		1434.3	5.24×10^4	1438.4	1.23×10^4
B	$1s2s^22p^3$	1		1434.3	3.23×10^4	1438.4	8.81×10^3
B	$1s2s^22p^3$	1		1438.1	1.74×10^4	1442.0	6.80×10^3
B	$1s2s^22p^3$	2		1438.5	4.38×10^4	1442.4	7.09×10^3
B	$1s2s^22p^3$	0		1438.6	8.15×10^3	1442.5	1.75×10^3
B	$1s2s^22p^3$	1		1438.8	2.72×10^4	1442.8	7.07×10^3
B	$1s2s^22p^3$	2	TR	1443.6	9.52×10^4	1447.7	2.36×10^4
B	$1s2s^22p^3$	1	TR	1447.8	4.81×10^4	1451.6	1.41×10^4
B	$1s2p^5$	2	QR	1521.6	1.56×10^3	1521.9	1.38×10^{-1}
B	$1s2p^5$	1	QR	1522.2	8.73×10^2	1522.6	8.80
B	$1s2p^5$	0	QR	1522.7	2.71×10^2	1523.1	4.74
B	$1s2p^5$	1	QR	1531.2	1.66×10^3	1531.2	1.12×10^1

TABLE VIII. Same as Table VI for C-, N-, and O-like ions.

				MCDF results		FAC results	
$\|i\rangle$	$\|d\rangle$	J	HO	E_e (eV)	S^{rec} (b eV)	E_e (eV)	S^{rec} (b eV)
C	$1s2s^22p^4$	5/2		1468.0	8.29×10^4	1469.4	1.04×10^4
C	$1s2s^22p^4$	3/2		1468.7	2.01×10^4	1470.1	1.19×10^3
C	$1s2s^22p^4$	1/2		1468.9	1.46×10^4	1470.4	1.46×10^3
C	$1s2s^22p^4$	5/2	TR	1478.8	6.78×10^4	1480.3	5.54
C	$1s2s^22p^4$	3/2	TR	1478.9	6.90×10^4	1480.4	5.16×10^2
C	$1s2s^22p^4$	3/2	TR	1480.9	5.38×10^4	1482.6	2.25×10^4
C	$1s2s^22p^4$	1/2	TR	1481.3	1.46×10^4	1483.1	3.17×10^3
C	$1s2s^22p^4$	1/2	QR	1485.0	2.98×10^4	1486.4	9.99×10^{-1}
C	$1s2p^6$	1/2	QR	1573.7	1.92×10^3	1574.4	8.43×10^{-2}
N	$1s2s^22p^5$	2		1509.8	3.81×10^4	1512.5	7.57
N	$1s2s^22p^5$	1		1510.4	1.67×10^4	1513.1	4.41
N	$1s2s^22p^5$	1	TR	1517.9	3.02×10^4	1520.8	1.28×10^1
O	$1s2s^22p^6$	1/2		1538.9	1.67×10^4	1540.9	3.28×10^1

TABLE IX. Resonance energies E_e and resonance strengths S^{rec} for resonant recombination into metastable states of Be-like silicon ions according to MCDF and FAC calculations. See the caption of Table IV for the notation.

				MCDF results		FAC results	
Ion	$\|i\rangle$	$\|d\rangle$	J	E_e (eV)	S^{rec} (b eV)	E_e (eV)	S^{rec} (b eV)
Be	$1s^22s2p\,^3P_0^o$	$1s2s2p2p^2$	1/2	1374.8	1.33×10^3	1373.9	1.05×10^2
Be	$1s^22s2p\,^3P_0^o$	$1s2s2p2p^2$	3/2	1375.3	2.56×10^3	1374.3	4.67×10^2
Be	$1s^22s2p\,^3P_0^o$	$1s2s2p2p^2$	5/2	1375.7	6.95×10^{-1}	1374.7	0.04×10^{-1}
Be	$1s^22s2p\,^3P_0^o$	$1s2s2p2p^2$	5/2	1386.9	1.14	1386.1	1.31×10^1
Be	$1s^22s2p\,^3P_0^o$	$1s2s2p2p^2$	3/2	1387.1	2.40×10^4	1386.3	2.61×10^3
Be	$1s^22s2p\,^3P_0^o$	$1s2s2p2p^2$	1/2	1389.2	4.56×10^3	1388.7	5.31×10^2
Be	$1s^22s2p\,^3P_0^o$	$1s2s2p2p^2$	3/2	1390.1	6.24×10^3	1389.6	1.28×10^3
Be	$1s^22s2p\,^3P_0^o$	$1s2s2p2p^2$	1/2	1393.0	7.19×10^3	1392.3	7.87×10^2
Be	$1s^22s2p\,^3P_0^o$	$1s2p^4$	5/2	1445.0	1.19×10^{-2}	1444.5	0.02×10^{-2}
Be	$1s^22s2p\,^3P_0^o$	$1s2p^4$	3/2	1445.7	4.31×10^3	1445.2	3.19×10^2
Be	$1s^22s2p\,^3P_0^o$	$1s2p^4$	1/2	1446.0	1.01×10^3	1445.5	7.36×10^1
Be	$1s^22s2p\,^3P_0^o$	$1s2p^4$	5/2	1456.9	2.83×10^{-2}	1456.4	0.03
Be	$1s^22s2p\,^3P_0^o$	$1s2p^4$	3/2	1457.0	8.62×10^2	1456.6	8.47×10^1
Be	$1s^22s2p\,^3P_0^o$	$1s2p^4$	3/2	1459.6	3.46×10^1	1459.2	6.96
Be	$1s^22s2p\,^3P_0^o$	$1s2p^4$	1/2	1460.2	1.22×10^2	1459.7	2.64×10^1
Be	$1s^22s2p\,^3P_0^o$	$1s2p^4$	1/2	1471.6	5.19×10^2	1471.2	6.89×10^1

TABLE X. Same as Table IX for B-like ions.

				MCDF results		FAC results	
Ion	$\|i\rangle$	$\|d\rangle$	J	E_e (eV)	S^{rec} (b eV)	E_e (eV)	S^{rec} (b eV)
B	$1s^2 2s^2 2p\ ^2P^o_{3/2}$	$1s2s^2 2p^3$	2	1419.0	4.47×10^1	1423.2	0.02
B	$1s^2 2s^2 2p\ ^2P^o_{3/2}$	$1s2s^2 2p^3$	3	1433.3	3.90×10^4	1437.4	1.39×10^4
B	$1s^2 2s^2 2p\ ^2P^o_{3/2}$	$1s2s^2 2p^3$	2	1433.4	2.62×10^4	1437.6	6.58×10^3
B	$1s^2 2s^2 2p\ ^2P^o_{3/2}$	$1s2s^2 2p^3$	1	1433.4	1.52×10^4	1437.6	3.27×10^3
B	$1s^2 2s^2 2p\ ^2P^o_{3/2}$	$1s2s^2 2p^3$	1	1437.2	1.73×10^4	1441.2	8.98×10^3
B	$1s^2 2s^2 2p\ ^2P^o_{3/2}$	$1s2s^2 2p^3$	2	1437.6	2.59×10^4	1441.5	9.46×10^3
B	$1s^2 2s^2 2p\ ^2P^o_{3/2}$	$1s2s^2 2p^3$	0	1437.7	5.13×10^3	1441.7	1.68×10^3
B	$1s^2 2s^2 2p\ ^2P^o_{3/2}$	$1s2s^2 2p^3$	1	1437.9	2.21×10^4	1442.0	8.18×10^3
B	$1s^2 2s^2 2p\ ^2P^o_{3/2}$	$1s2s^2 2p^3$	2	1442.7	6.67×10^4	1446.8	2.96×10^4
B	$1s^2 2s^2 2p\ ^2P^o_{3/2}$	$1s2s^2 2p^3$	1	1446.9	3.51×10^4	1450.8	1.66×10^4
B	$1s^2 2s^2 2p\ ^2P^o_{3/2}$	$1s2p^5$	2	1520.7	8.75×10^2	1521.1	1.25×10^1
B	$1s^2 2s^2 2p\ ^2P^o_{3/2}$	$1s2p^5$	1	1521.4	5.30×10^2	1521.7	2.92
B	$1s^2 2s^2 2p\ ^2P^o_{3/2}$	$1s2p^5$	0	1521.8	1.76×10^2	1522.2	0.03
B	$1s^2 2s^2 2p\ ^2P^o_{3/2}$	$1s2p^5$	1	1530.3	1.16×10^3	1530.4	9.75

TABLE XI. Same as Table IX for C-like ions.

				MCDF results		FAC results	
Ion	$\|i\rangle$	$\|d\rangle$	J	E_e (eV)	S^{rec} (b eV)	E_e (eV)	S^{rec} (b eV)
C	$1s^2 2s^2 2p^2\ ^1D_2$	$1s2s^2 2p^4$	5/2	1463.5	1.81×10^4	1462.6	1.41×10^1
C	$1s^2 2s^2 2p^2\ ^1D_2$	$1s2s^2 2p^4$	3/2	1464.2	1.32×10^4	1463.3	1.93×10^1
C	$1s^2 2s^2 2p^2\ ^1D_2$	$1s2s^2 2p^4$	1/2	1464.4	7.14×10^3	1463.5	3.86
C	$1s^2 2s^2 2p^2\ ^1D_2$	$1s2s^2 2p^4$	5/2	1474.3	4.51×10^4	1473.5	2.67×10^4
C	$1s^2 2s^2 2p^2\ ^1D_2$	$1s2s^2 2p^4$	3/2	1474.4	3.21×10^4	1473.6	1.78×10^4
C	$1s^2 2s^2 2p^2\ ^1D_2$	$1s2s^2 2p^4$	3/2	1476.4	1.52×10^4	1475.8	1.81×10^3
C	$1s^2 2s^2 2p^2\ ^1D_2$	$1s2s^2 2p^4$	1/2	1476.8	1.85×10^4	1476.2	2.84×10^2
C	$1s^2 2s^2 2p^2\ ^1D_2$	$1s2s^2 2p^4$	1/2	1480.5	1.37×10^4	1479.6	6.91×10^3
C	$1s^2 2s^2 2p^2\ ^1D_2$	$1s2p^6$	1/2	1569.2	2.29×10^3	1567.5	0.02
C	$1s^2 2s^2 2p^2\ ^1S_0$	$1s2s^2 2p^4$	5/2	1456.3	5.70×10^4	1456.5	4.10
C	$1s^2 2s^2 2p^2\ ^1S_0$	$1s2s^2 2p^4$	3/2	1457.0	9.46×10^3	1457.2	1.60×10^{-2}
C	$1s^2 2s^2 2p^2\ ^1S_0$	$1s2s^2 2p^4$	1/2	1457.3	6.44×10^3	1457.4	3.41
C	$1s^2 2s^2 2p^2\ ^1S_0$	$1s2s^2 2p^4$	5/2	1467.2	1.24×10^5	1467.4	1.70×10^4
C	$1s^2 2s^2 2p^2\ ^1S_0$	$1s2s^2 2p^4$	3/2	1467.3	6.77×10^4	1467.5	1.11×10^4
C	$1s^2 2s^2 2p^2\ ^1S_0$	$1s2s^2 2p^4$	3/2	1469.2	7.99×10^4	1469.7	1.73×10^3
C	$1s^2 2s^2 2p^2\ ^1S_0$	$1s2s^2 2p^4$	1/2	1469.7	3.13×10^2	1470.1	7.51×10^2
C	$1s^2 2s^2 2p^2\ ^1S_0$	$1s2s^2 2p^4$	1/2	1473.4	5.30×10^4	1473.5	1.64×10^4
C	$1s^2 2s^2 2p^2\ ^1S_0$	$1s2p^6$	1/2	1562.0	4.21×10^3	1561.4	3.65×10^1

TABLE XII. Same as Table IX for N- and O-like ions.

				MCDF results		FAC results	
Ion	$\|i\rangle$	$\|d\rangle$	J	E_e (eV)	S^{rec} (b eV)	E_e (eV)	S^{rec} (b eV)
N	$1s^2 2s^2 2p^3\ ^2D^o_{3/2}$	$1s2s^2 2p^5$	2	1501.5	2.71×10^4	1503.6	7.35×10^3
N	$1s^2 2s^2 2p^3\ ^2D^o_{3/2}$	$1s2s^2 2p^5$	1	1502.1	1.96×10^4	1504.2	5.31×10^3
N	$1s^2 2s^2 2p^3\ ^2D^o_{3/2}$	$1s2s^2 2p^5$	0	1502.5	6.88×10^3		
N	$1s^2 2s^2 2p^3\ ^2D^o_{3/2}$	$1s2s^2 2p^5$	1	1509.6	2.63×10^4	1511.9	1.01×10^4
N	$1s^2 2s^2 2p^3\ ^2D^o_{5/2}$	$1s2s^2 2p^5$	2	1503.2	2.83×10^4	1503.5	9.50×10^3
N	$1s^2 2s^2 2p^3\ ^2D^o_{5/2}$	$1s2s^2 2p^5$	1	1503.8	1.62×10^4	1504.1	4.17×10^3
N	$1s^2 2s^2 2p^3\ ^2D^o_{5/2}$	$1s2s^2 2p^5$	0	1504.3	5.12×10^3		
N	$1s^2 2s^2 2p^3\ ^2D^o_{5/2}$	$1s2s^2 2p^5$	1	1511.4	2.84×10^4	1511.9	1.00×10^4
N	$1s^2 2s^2 2p^3\ ^2P^o_{1/2}$	$1s2s^2 2p^5$	2	1497.2	5.71×10^4	1499.6	6.68×10^3
N	$1s^2 2s^2 2p^3\ ^2P^o_{1/2}$	$1s2s^2 2p^5$	1	1497.8	3.09×10^4	1500.2	3.98×10^3
N	$1s^2 2s^2 2p^3\ ^2P^o_{1/2}$	$1s2s^2 2p^5$	0	1498.2	9.25×10^3	1500.6	1.29×10^3
N	$1s^2 2s^2 2p^3\ ^2P^o_{1/2}$	$1s2s^2 2p^5$	1	1505.3	4.38×10^4	1507.9	8.17×10^3
N	$1s^2 2s^2 2p^3\ ^2P^o_{3/2}$	$1s2s^2 2p^5$	2	1501.5	1.68×10^4	1499.5	5.38×10^3
N	$1s^2 2s^2 2p^3\ ^2P^o_{3/2}$	$1s2s^2 2p^5$	1	1502.1	2.32×10^4	1500.1	4.67×10^3
N	$1s^2 2s^2 2p^3\ ^2P^o_{3/2}$	$1s2s^2 2p^5$	0	1502.5	8.34×10^3	1500.5	1.84×10^3
N	$1s^2 2s^2 2p^3\ ^2P^o_{3/2}$	$1s2s^2 2p^5$	1	1509.6	3.35×10^4	1507.8	8.49×10^3
O	$1s^2 2s^2 2p^4\ ^1D_2$	$1s2s^2 2p^6$	1/2	1536.3	1.85×10^4	1535.0	1.35×10^4
O	$1s^2 2s^2 2p^4\ ^1S_0$	$1s2s^2 2p^6$	1/2	1531.2	4.16×10^4	1529.1	7.81×10^3

[1] A. Burgess, Astrophys. J. **139**, 776 (1964).
[2] P. Auger, J. Phys. Radium **6**, 205 (1925).
[3] M. Schnell, G. Gwinner, N. R. Badnell, M. E. Bannister, S. Böhm, J. Colgan, S. Kieslich, S. D. Loch, D. Mitnik, A. Müller, M. S. Pindzola, S. Schippers, D. Schwalm, W. Shi, A. Wolf, and S.-G. Zhou, Phys. Rev. Lett. **91**, 043001 (2003).
[4] C. Beilmann, O. Postavaru, L. H. Arntzen, R. Ginzel, C. H. Keitel, V. Mäckel, P. H. Mokler, M. C. Simon, H. Tawara, I. I. Tupitsyn, J. Ullrich, J. R. Crespo López-Urrutia, and Z. Harman, Phys. Rev. A **80**, 050702 (2009).
[5] C. Beilmann, P. H. Mokler, S. Bernitt, C. H. Keitel, J. Ullrich, J. R. Crespo López-Urrutia, and Z. Harman, Phys. Rev. Lett. **107**, 143201 (2011).
[6] C. Beilmann, Z. Harman, P. H. Mokler, S. Bernitt, C. H. Keitel, J. Ullrich, and J. R. Crespo López-Urrutia, Phys. Rev. A **88**, 062706 (2013).
[7] B. F. Rozsnyai, Astrophys. J. **393**, 409 (1992).
[8] P. Bryans, N. R. Badnell, T. W. Gorczyca, J. M. Laming, W. Mitthumsiri, and D. W. Savin, Astrophys. J. Suppl. Ser. **167**, 343 (2006).
[9] C. Blancard, P. Cossé, and G. Faussurier, Astrophys. J. **745**, 10 (2012).
[10] J. E. Bailey, G. A. Rochau, R. C. Mancini, C. A. Iglesias, J. J. MacFarlane, I. E. Golovkin, C. Blancard, Ph. Cosse, and G. Faussurier, Phys. Plasmas **16**, 058101 (2009).
[11] L. H. Andersen, G. Y. Pan, H. T. Schmidt, M. S. Pindzola, and N. R. Badnell, Phys. Rev. A **45**, 6332 (1992).
[12] L. H. Andersen, G.-Y. Pan, H. T. Schmidt, N. R. Badnell, and M. S. Pindzola, Phys. Rev. A **45**, 7868 (1992).
[13] T. Bartsch, A. Müller, W. Spies, J. Linkemann, H. Danared, D. R. DeWitt, H. Gao, W. Zong, R. Schuch, A. Wolf, G. H. Dunn, M. S. Pindzola, and D. C. Griffin, Phys. Rev. Lett. **79**, 2233 (1997).
[14] E. W. Schmidt, D. Bernhardt, A. Müller, S. Schippers, S. Fritzsche, J. Hoffmann, A. S. Jaroshevich, C. Krantz, M. Lestinsky, D. A. Orlov, A. Wolf, D. Lukić, and D. W. Savin, Phys. Rev. A **76**, 032717 (2007).
[15] I. Orban, E. Lindroth, P. Glans, and R. Schuch, J. Phys. B **40**, 1063 (2007).
[16] I. Orban, S. D. Loch, S. Böhm, and R. Schuch, Astrophys. J. **721**, 1603 (2010).
[17] J. Kenntner, J. Linkemann, N. R. Badnell, C. Broude, D. Habs, G. Hofmann, A. Müller, M. S. Pindzola, E. Salzborn, D. Schwalm, and A. Wolf, Nucl. Instrum. Methods Phys. Res. B **98**, 142 (1995).
[18] S. Ali, I. Orban, S. Mahmood, S. Tashenov, and R. Schuch, J. Phys. Conf. Ser. **194**, 062021 (2009).
[19] H. G. Wei *et al.*, Astrophys. J. **683**, 577 (2008).
[20] Y. Hahn, Rep. Prog. Phys. **60**, 691 (1997).
[21] Z. Harman, I. I. Tupitsyn, A. N. Artemyev, U. D. Jentschura, C. H. Keitel, J. R. Crespo López-Urrutia, A. J. González Martínez, H. Tawara, and J. Ullrich, Phys. Rev. A **73**, 052711 (2006).
[22] P. Zimmerer, N. Grün, and W. Scheid, Phys. Lett. A **148**, 457 (1990).
[23] K. G. Dyall, I. P. Grant, C. T. Johnson, F. A. Parpia, and E. P. Plummer, Comput. Phys. Commun. **55**, 425 (1989).
[24] M. F. Gu, Astrophys. J. **590**, 1131 (2003).
[25] M. F. Gu, Can. J. Phys. **86**, 675 (2008).
[26] E. Träbert, M. Grieser, J. Hoffmann, C. Krantz, R. Repnow, and A. Wolf, Phys. Rev. A **85**, 042508 (2012).

[27] D. A. Knapp, R. E. Marrs, M. A. Levine, C. L. Bennett, M. H. Chen, J. R. Henderson, M. B. Schneider, and J. H. Scofield, Phys. Rev. Lett. **62**, 2104 (1989).

[28] T. Fuchs, C. Biedermann, R. Radtke, E. Behar, and R. Doron, Phys. Rev. A **58**, 4518 (1998).

[29] A. J. González Martínez, J. R. Crespo López-Urrutia, J. Braun, G. Brenner, H. Bruhns, A. Lapierre, V. Mironov, R. Soria Orts, H. Tawara, M. Trinczek, J. Ullrich, and J. H. Scofield, Phys. Rev. Lett. **94**, 203201 (2005).

[30] B. M. Penetrante, J. N. Bardsley, D. DeWitt, M. Clark, and D. Schneider, Phys. Rev. A **43**, 4861 (1991).

[31] G. Liang, J. R. Crespo López-Urrutia, T. M. Baumann, S. W. Epp, A. Gonchar, A. Lapierre, P. H. Mokler, M. C. Simon, H. Tawara, V. Mäckel, K. Yao, G. Zhao, Y. Zou, and J. Ullrich, Astrophys. J. **702**, 838 (2009).

[32] M. Klapisch, Shalom, J. L. Schwob, B. S. Fraenkel, C. Breton, C. de Michelis, M. Finkenthal, and M. Mattioli, Phys. Lett. **69A**, 34 (1978).

[33] L. J. Roszman, Phys. Rev. A **39**, 2073 (1989).